Temperature Dependency of Hydrogen Embrittlement in Thermally H-precharged STS 304 Austenitic Stainless Steel

Hanna Yang[1,2] · Thanh Tuan Nguyen[1] · Jaeyeong Park[1] · Hyeong Min Heo[1] · Junghoon Lee[2] · Un Bong Baek[1] · Young-Kook Lee[2,3]

Abstract

In the present study, the resistance to hydrogen embrittlement (HE) of STS 304 austenitic stainless steel was investigated at a wide range of temperature from 25 to − 253 °C. Tensile specimens were thermally precharged with H at 300 °C for 35 days under a H_2 gas pressure of 10 MPa. The resistance to HE was reduced with decreasing tensile temperature from 25 to − 50 °C, and then increased again with decreasing deformation temperature further. Finally, HE disappeared at temperatures below − 150 °C. This temperature dependency of HE in thermally H-precharged specimens was almost the same as that in the specimens deformed in a H_2 gaseous environment. The occurrence of HE at the temperature range of 25 to − 50 °C was attributed to both strain-induced martensitic transformation (SIMT) and H diffusion into stress-concentrated regions. The absence of HE at temperatures below − 150 °C was due to the sluggish H diffusion, despite of active SIMT.

Keywords 304 austenitic stainless steel · Hydrogen embrittlement · Slow strain rate tensile test · Strain-induced -martensite

1 Introduction

In recent years, the interest in a hydrogen (H)-fueled vehicle is rapidly increasing. One of current issues is an increase in energy density by liquefying a H_2 gas for the safety and efficiency of storage and transportation. Because the liquefaction temperature of a H_2 gas is ~ − 253 °C, a material for a liquid H container must possess a high resistance to hydrogen embrittlement (HE) at low temperatures ranging from room temperature to − 253 °C. For this purpose, type 304 austenitic stainless steel (STS 304) has been extensively

studied and used as a low-temperature material due to its high low-temperature toughness [1, 2], fatigue strength [3] and corrosion resistance [4, 5].

Meanwhile, the resistance to HE of STS 304 at a low temperature was mostly investigated using the specimens exposed to a H_2 gaseous environment. Han et al. [6] investigated the effects of carbide and strain-induced α′-martensite on HE at temperatures ranging from room temperature to − 193 °C through slow strain rate tensile tests (SSRTs) in H_2 and He gases using solution-annealed, sensitized, and desensitized STS 304 specimens. Regardless of heat treatment condition, the resistance to HE was the lowest at ~ − 53 °C, which was related to the formation of strain-induced α′-martensite along grain boundaries. Michler et al. [7] examined the effect of H_2 gas pressure on the resistance to HE of STS 304 at temperatures ranging from 20 to − 80 °C through SSRTs. The resistance to HE was lowered when the pressure of a H_2 gas increased and tensile temperature decreased. Sun et al. [8] studied the effect of tensile strain rate on the resistance to HE using STS 304 specimens in a H_2 gas atmosphere at temperatures ranging from 26 to − 196 °C. HE was not observed at an initial strain rate of 4.2×10^{-2} s^{-1}, regardless of deformation temperature. However, when the initial strain rate decreased to 4.2×10^{-3} s^{-1}, HE occurred and became severe with decreasing the initial

✉ Un Bong Baek
  ubbaek@kriss.re.kr

✉ Young-Kook Lee
  yklee@yonsei.ac.kr

1   Division of Industrial Metrology, Center for Energy Materials Measurement, Korea Research Institute of Standard and Science (KRISS), Daejeon 34113, Republic of Korea

2   Department of Materials Science and Engineering, Yonsei University, Seoul 03722, Republic of Korea

3   Graduate Institute of Ferrous & Energy Materials Technology, Pohang University of Science and Technology, Pohang 37673, Republic of Korea

strain rate further. HE was the most severe at -73 °C, and disappeared at temperatures below -123 °C.

Unlike reports mentioned above, there are only a few studies on the resistance to HE of H- precharged STS 304 specimens at low temperatures. Nam et al. [9] examined the effect of deformation temperature on the resistance to HE using H-precharged STS 304 specimens. The specimens were H-charged at 300 °C for 8 days under a H_2 gas pressure of 10 MPa, and then tensile deformed at temperatures ranging from room temperature to -80 °C. The resistance to HE was gradually reduced to -20 °C, and then recovered at temperatures below -20 °C. However, until now the resistance to HE of H-precharged STS 304 was scarcely investigated at low temperatures ranging from -80 to -253 °C. Therefore, the objective of the present study is to evaluate the resistance to HE of thermally H-precharged STS 304 at a wide temperature range from room temperature (25 °C) to -253 °C through SSRTs. In addition, by comparing present results to previous ones obtained in a H_2 gas atmosphere, the effect of H-charging condition on the resistance to HE at low temperatures is also discussed.

2 Experimental Procedure

For present study, a hot-rolled STS 304 plate with a thickness of 16 mm was used. The chemical composition of the plate was measured using an optical emission spectroscope (OES; Thermo Scientific, ARL4460) and a NO analyzer (LECO, ON836), and is listed in Table 1. The microstructure of the hot-rolled plate consisted of γ austenite (96%) and δ-ferrite (4%), as shown in Fig. 1. The average size of γ austenite grains was 26.3 µm. For SSRTs, round-type tensile specimens with a gauge portion of 6.0 mm in diameter and 28.6 mm long were machined along the transverse direction of the plate by lathe processing [10].

To investigate the resistance to HE, SSRT specimens were thermally H-charged at 300 °C for 35 days under a H_2 gas pressure of 10 MPa. The H charging time was determined according to the instruction of CSA/CSCM 1—2014 [11]. The H-precharged specimens were stored in a fridge of -70 °C to prevent the outgassing of H before SSRTs. The SSRTs of both H-precharged and uncharged specimens were performed using a servo-hydraulic tensile tester equipped with a cryo-cooler under an air condition at temperatures ranging from 25 to -253 °C. Tensile specimens were deformed with a strain rate of 2×10^{-5} s^{-1} at temperatures

above -150 °C, and 2×10^{-4} s^{-1} at -196 °C and -253 °C due to technical limits. The ratio of the reduction of area (RA) was evaluated by measuring the diameter of a gauge part before and after the SSRT using a micrometer.

The H contents of H-uncharged and precharged specimens were measured using a thermal desorption spectroscope (TDS; R-DEC, HTDS-003) with a Q-mass detector. TDS specimens measuring 6 mm in diameter and 2 mm thick were taken at the middle of the gauge part. The TDS specimens were heated at a constant rate of 100 °C/h from 25 to 900 °C. The H content of each specimen was converted from the area of a H desorption rate curve.

To measure the H diffusivity of α' martensite, which forms and is deformed during tensile deformation, a hot-rolled plate of STS 304L with a chemical composition in Table 1 was cryo-rolled at -196 °C from 2.0 to 0.7 mm, corresponding to a thickness reduction of 65%. STS 304L was adopted because it has a higher volume fraction of α' martensite after cryo-rolling than STS 304 due to the less C content.

The cryo-rolled STS 304L specimen consisted of 98.5% α' martensite and 1.5% γ, as seen in Fig. 2. The diffusivity of H in the α' martensite of STS 304L specimen was measured by means of electrochemical H permeation testing. The test was performed at 25 °C using two potentiostats (Gamry Instruments, Interface 1010E). The permeation test system was composed of a set of cathodic (H charging) and anodic (H detection) cells. A test sample was located in between the two cells. Rectangular-shaped specimens measuring 20 mm $\times$ 20 mm were mechanically polished with #2000 grit SiC paper to a thickness of 1.00 ± 0.05 mm. To prevent the oxidation of a specimen [12] and improve the H oxidation reaction (H $\rightarrow$ H$^+$ + e$^-$) [13] during the permeation test, the anodic side of the specimen was coated with Pd using an ion coater. The thickness of the Pd coating layer was ~ 50 nm. The diameter of the test sample was 11 mm. The specimens were cathodically H-charged using a 3 wt% NaCl aqueous solution containing 0.3 wt% NH_4SCN at a current density of 5 Am^{-2}. The H detection was carried out at a constant potential of $+250$ mV using a Ag/AgCl/3 M KCl reference electrode in the 0.1 M NaOH solution. Solutions in both cathodic and anodic cells were continuously purged by an Ar gas with a purity of 99.999% during the permeation test.

The microstructures of fractured specimens were observed using a scanning electron microscope (SEM; JEOL, JSM-7100F) equipped with an electron backscatter diffractometer (EBSD; OXFORD, NordlysNano). For

Table 1 Chemical compositions of STS 304 and STS 304L

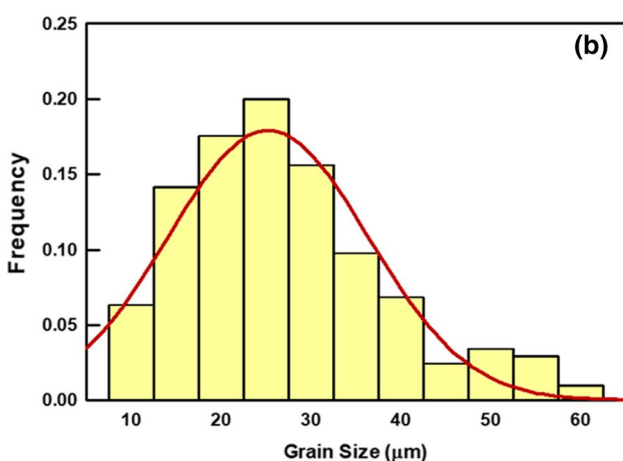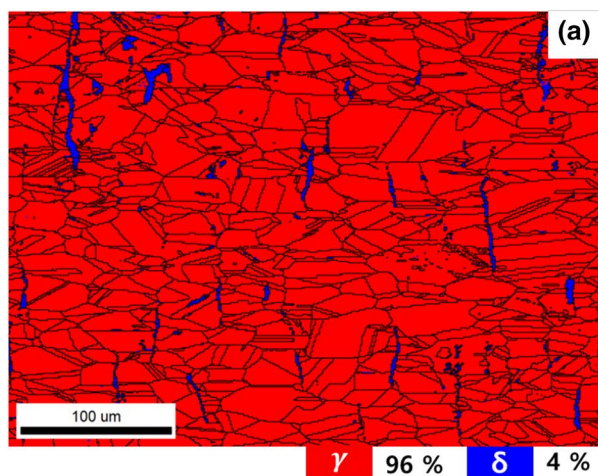| Element (wt%)	C	Si	Mn	Cr	Ni	Cu	Mo	Co	N
STS 304	0.050	0.51	0.93	18.1	8.02	0.26	0.16	0.22	0.0375
STS 304L	0.017	0.38	1.63	18.2	8.04	0.25	0.13	0.22	0.0381

Fig. 1 **a** EBSD phase map of a hot-rolled specimen and **b** a distribution of γ grain size

Fig. 2 X-ray diffraction pattern of STS 304L specimen cryo-rolled at −196 ℃ with a reduction ratio of 65%

EBSD observation, a cross-sectional area of a fractured specimen was mechanically polished, followed by electro-etching using a 10% oxalic acid to remove surface defects. The EBSD was performed with an acceleration voltage of 19 kV and a step size of 0.3 μm. The phase fractions of fractured specimens were measured using an X-ray dif-fractometer (XRD; RIGAKU, SmartLab) with a Cu-K α radiation, operating at a voltage of 45 kV and a current of 200 mA. X-ray diffraction (XRD) tests were conducted using the EBSD specimens. The scanning range and rate were 40°–100° and 5° min^{-1}. The quantitative analysis of phase fractions was performed using a reference intensity ratio in SmartLab Studio [14].
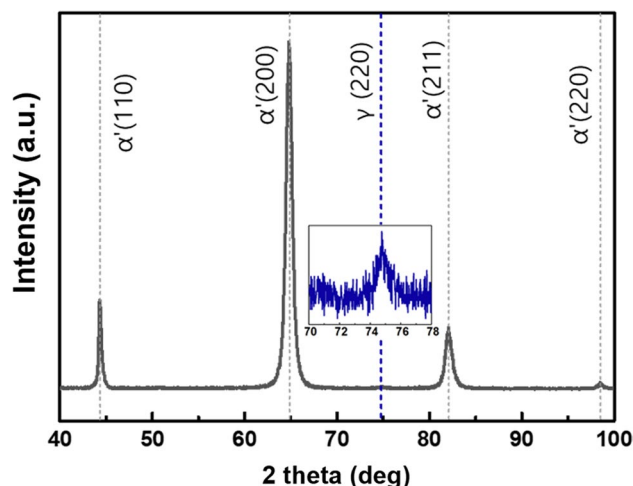
3 Experimental Results

Figure 3 shows H desorption rate curves measured before tensile tests using H-uncharged and precharged specimens. The H contents of H-uncharged and precharged specimens were 1.63 mass ppm and 43.72 mass ppm, respectively. The peak temperature of H-precharged specimen was ∼480 °C, which is higher than that (∼140 °C) of an electrochemically H-charged specimen. This is because electrochemical charg-ing induces a steep gradient of H concentration near the sur-face whereas thermal H charging H makes a homogeneous H distributed in the specimen [15].

Figure 4 shows tensile stress-train curves of H-uncharged and precharged STS 304 specimens, which were twice measured through SSRTs at various temperatures from 25 to −253 °C. High strain hardening was observed in the ten-sile curves measured at subzero temperatures most likely due to active strain-induced α′ martensitic transformation (SIMT) [16]. As seen in Fig. 4a–c, the elongation of H-pre-charged specimens was greatly decreased at 25 °C, −50 °C and −100 °C, indicating the occurrence of HE. However, at temperatures below -150 °C (Fig. 4d–f), the reduction of elongation by H precharging was not observed, which means the absence of HE.

Tensile properties, such as yield strength (YS), ultimate tensile strength (UTS) and elongation of H-uncharged and precharged specimens were summarized in Fig. 5. Both YS and UTS increased with decreasing tensile temperature, regardless of H precharging (Fig. 5a and b). The increas-ing rate of UTS is higher than that of YS. The YSs of H-precharged specimens were slightly higher than those of H-unchanged specimens (Fig. 5a), most likely due to the solid solution hardening effect of H atoms [17]. At tensile temperatures above −100 °C, both UTS and elongation

were deteriorated by H precharging due to premature failure caused by HE. However, the values of UTS and elongation were little changed by H precharging at temperatures below − 150 °C, indicating the absence of HE.

To quantitatively evaluate the resistance to HE of STS 304, the relative reduction of area (RRA) values of the specimens deformed at various temperatures were calculated using the following equation.

$$RRA = RA_{H-precharged}/RA_{H-uncharged} \qquad (1)$$

where $RA_{H\text{-precharged}}$ and $RA_{H\text{-uncharged}}$ are the reduction of area (RA) values of H-precharged and uncharged specimens, which were calculated as follows.

$$RA(\%) = \frac{D_o - D_f}{D_o} \times 100 \qquad (2)$$

where D_o (= 6 mm) and D_f are the gauge diameters of an initial tensile specimen and a fractured specimen. The RA values of both H-uncharged and precharged specimens at various tensile temperatures were calculated and are plotted in Fig. 6a. The RA values of H-uncharged specimens were higher than those of H-precharged specimens at temperatures above − 100 °C. However, at temperatures below − 150 °C the RA values of H-uncharged and precharged specimens became similar.

Using the RA values and Eq. (1), the RRA values of specimens were calculated and are presented as a function of tensile temperature in Fig. 6b. With decreasing tensile temperature from 25 to − 50 °C, the RRA value of H-precharged specimens was decreased. This indicates that the resistance to HE was lowered with decreasing temperature. However, when tensile temperature decreased further, the RRA value increased again to reach ~ 1.0 at − 150 °C, implying the

Fig. 3 H desorption rate curves of H-uncharged and precharged specimens before SSRT

disappearance of HE. A slight decrease in the RRA value measured at − 196 and − 253 °C is probably due to the higher strain rate, as mentioned in experimental procedure. It is thought that a further study on the effect of strain rate on the RRA value is needed. For comparison, the RRA values of STS 304 specimens, which were deformed in a H_2 gas atmosphere under a pressure of 1 MPa [6], are presented together in Fig. 6b. The variation of the RRA values of the specimens deformed in a H_2 gas atmosphere with tensile temperature was similar to that of H-precharged specimens used in the present study. Therefore, it was found that the effect of H-charging condition on the temperature dependency of HE is insignificant.

To investigate a relationship between the temperature dependency of the RRA value and fracture mode, tensile-fractured specimens were observed using the SEM. Figure 7 provides SEM images of the fracture surfaces of H-uncharged specimens, which were deformed at 25, − 50, − 196 and − 253 °C. Regardless of tensile temperature, the fracture surfaces of H-uncharged specimens consisted of many dimples with a small amount of secondary cracks (yellow arrows) on relatively flat surfaces. The flat surfaces and secondary cracks are thought to be related to SIMT. It is noteworthy that the fracture surface of the specimen deformed at -253 °C revealed less secondary cracks and flat surfaces in spite of active SIMT (Fig. 7g and h). This result is closely related to the occurrence of serrations in the tensile flow curve (Fig. 3f). Koga et al. [18] studied the deformation behavior of a duplex stainless steel at cryogenic temperatures. They reported that, although the fracture mode changed from ductile to brittle with decreasing tensile temperature, ductile fracture reappeared at − 265 °C. They explained the transition of fracture mode from brittle to ductile at − 265 °C by the occurrence of serrations. Obst and Nyilas [19] and Ogata et al. [20] observed a series of thermal spites while serrations occurred by tensile deformation at cryogentic temperatures. The thermal spites increase the specimen temperature due to the low values of specific heat capacity and thermal conductivity at such low temperatures [21]. When the specimen temperature becomes higher than the ductile–brittle transition temperature of the specimen, resulting in ductile fracture. Therefore, it is thought that the enhancement of ductility in the specimen deformed at − 253 °C resulted from an increase in specimen temperature by the occurrence of serrations.

Figure 8 shows the fracture surfaces of H-precharged specimens, which were deformed at 25, − 50, − 196 and − 253 °C. Unlike H-uncharged specimens, Quasi-cleavage and transgranular fracture surfaces were observed in the specimens deformed at 25 and − 50 °C most likely due to HE. On the other hand, the fracture surfaces of H-precharged specimens, which failed at − 196 °C and − 253 °C without HE (Fig. 8e–h), were similar to those of H-uncharged
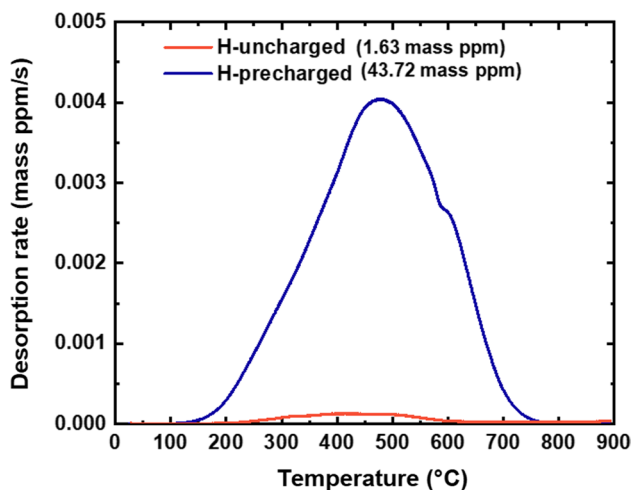
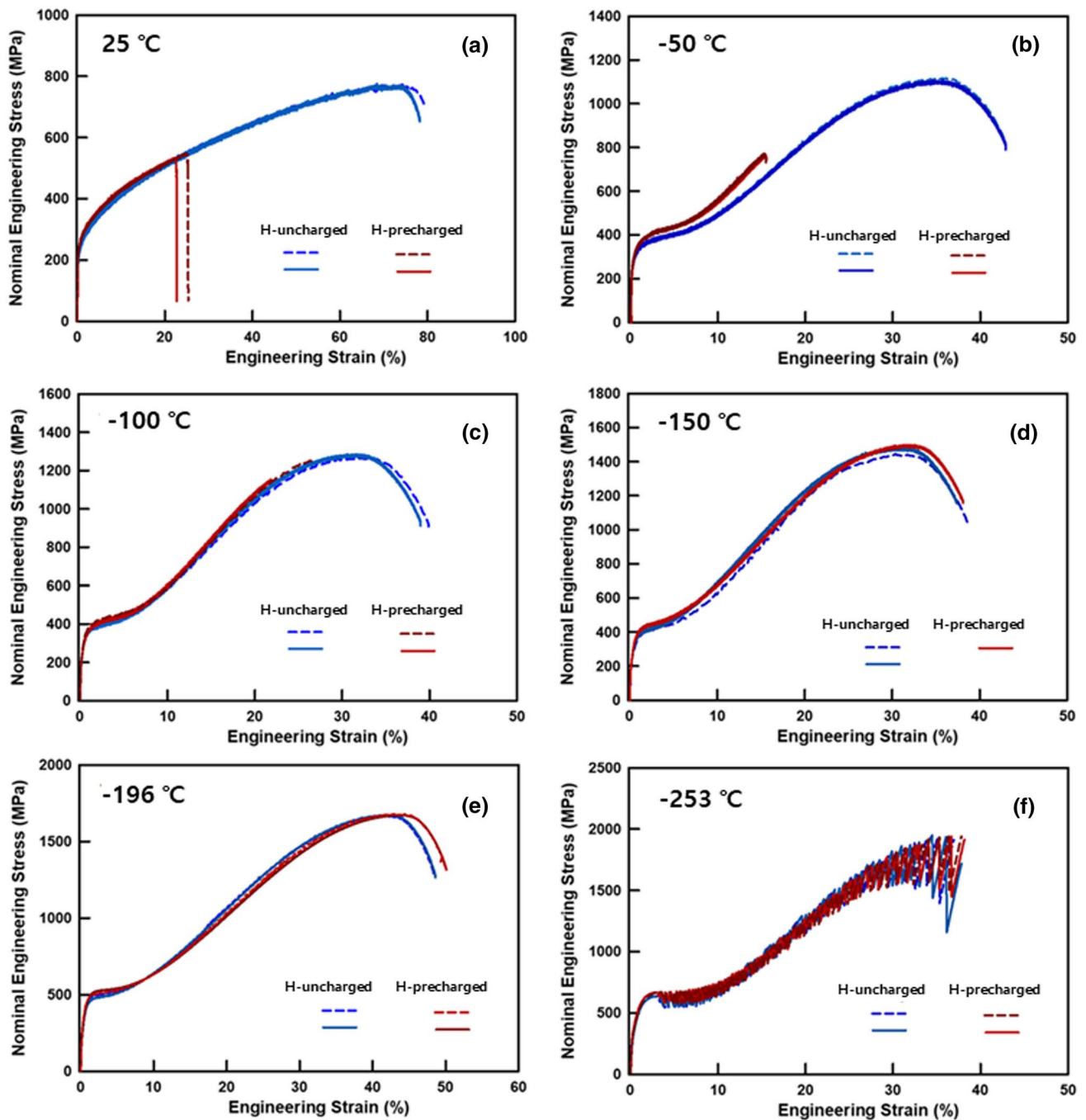**Fig. 4** Tensile stress–strain curves of H-uncharged and precharged specimens measured at various temperatures of **a** room temperature (25 °C), **b** − 50 °C, **c** − 100 °C, **d** − 150 °C, **e** − 196 °C and **f** − 253 °C

specimens failed at the same temperatures (Figs. 7e–h). Accordingly, the variation of fracture surface morphology with tensile temperature in both H-uncharged and precharged specimens shows good agreement with the temperature dependency of the RRA value.

Figure 9 shows inverse pole figure (IPF) and phase maps of H-precharged specimens deformed at 25 °C, − 50 °C and − 100 °C, which were taken near fracture tips. Fracture surfaces are indicated by white dotted lines, and α' martensite and γ phase are represented in blue and red colors on the phase maps. Although specimens were fractured at similar tensile strains (23% at 25 °C, 16% at − 50 °C, and 22% at − 100 °C), the volume fraction of α' martensite ($V_{\alpha'}$) was different; 36% at 25 °C, 53% at − 50 °C and 82%
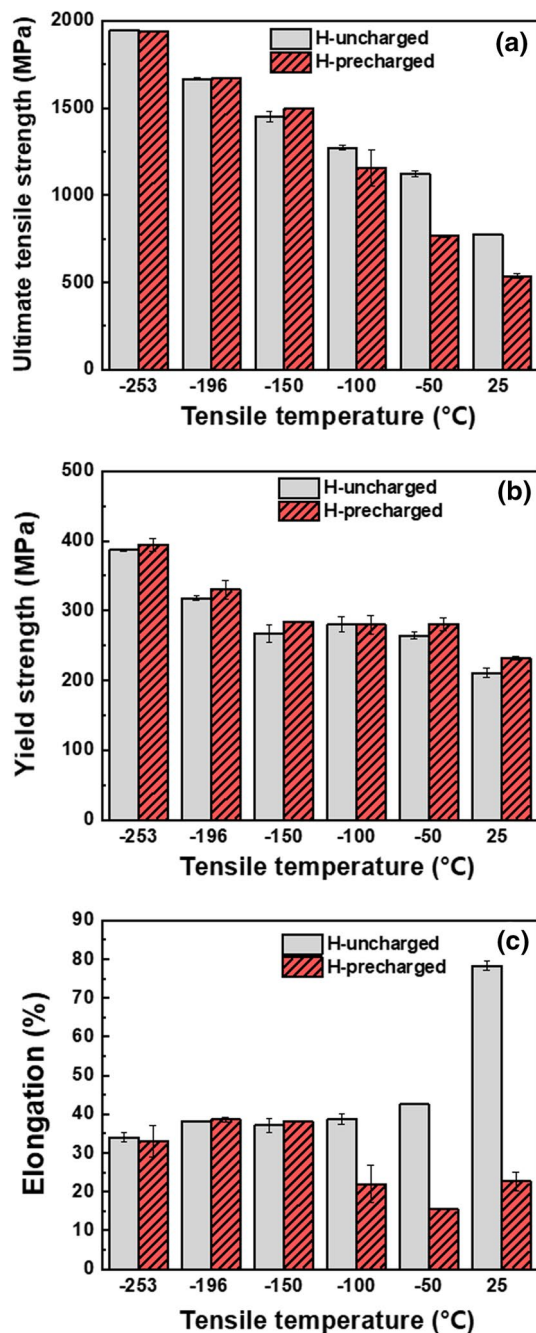
Fig. 5 Tensile properties of H-uncharged and precharged specimens measured at various temperatures; **a** yield strength (0.2% offset strength), **b** ultimate tensile strength and **c** elongation
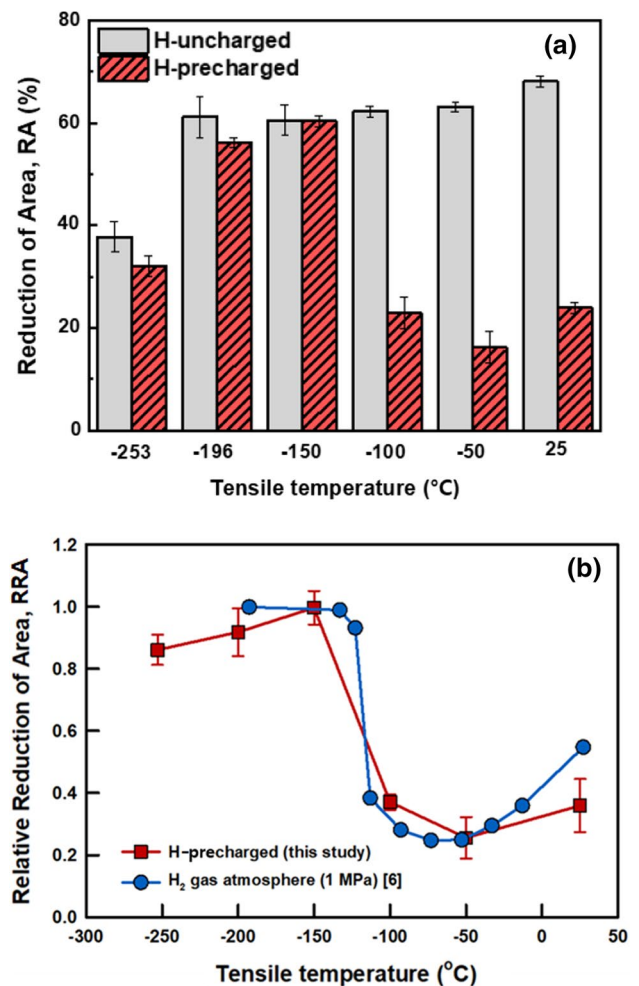

Fig. 6 Effects of tensile temperature on **a** the reduction of area values of H-uncharged and precharged specimens and **b** the relative reduction of area values of H-precharged specimens and specimens deformed in a H_2 gas atmosphere with a pressure of 1 MPa [6]

at −100 °C. Micro-cracks were observed in the specimens, which were deformed at −50 °C and −100 °C (black arrows in Fig. 9c–f). The cracks were initiated and grew in α' martensite. This confirms that α' martensite is vulnerable to HE.

4 Discussion

4.1 Temperature Dependency of HE

According to Han et al. [6], the reduction of the RRA value with decreasing tensile temperature from 25 to ~ −70 °C was due to the HE of hard martensite, which actively formed with decreasing tensile temperature. However, as tensile temperature was lowered further, the rate of H diffusion to stress-concentrated regions was decreased such that HE was alleviated in spite of active SIMT, and finally disappeared.

Therefore, in the present study SIMT was examined as a function of tensile tempearature. Figure 10a and b show X-ray diffraction patterns of H-uncharged and precharged specimens tensile- fractured at various temperatures. By applying the reference intensity ratio (RIR) method to the X-ray diffraction patterns, the $V_{\alpha'}$ values of fractured

Fig. 7 Fracture surfaces of H-uncharged specimens deformed at **a**, **b** 25 ℃, **c**, **d** − 50 ℃, **e**, **f** − 196 ℃ and **g**, **h** − 253 ℃. Yellow arrows in figures **b**, **d**, **f** and **h** indicate secondary cracks
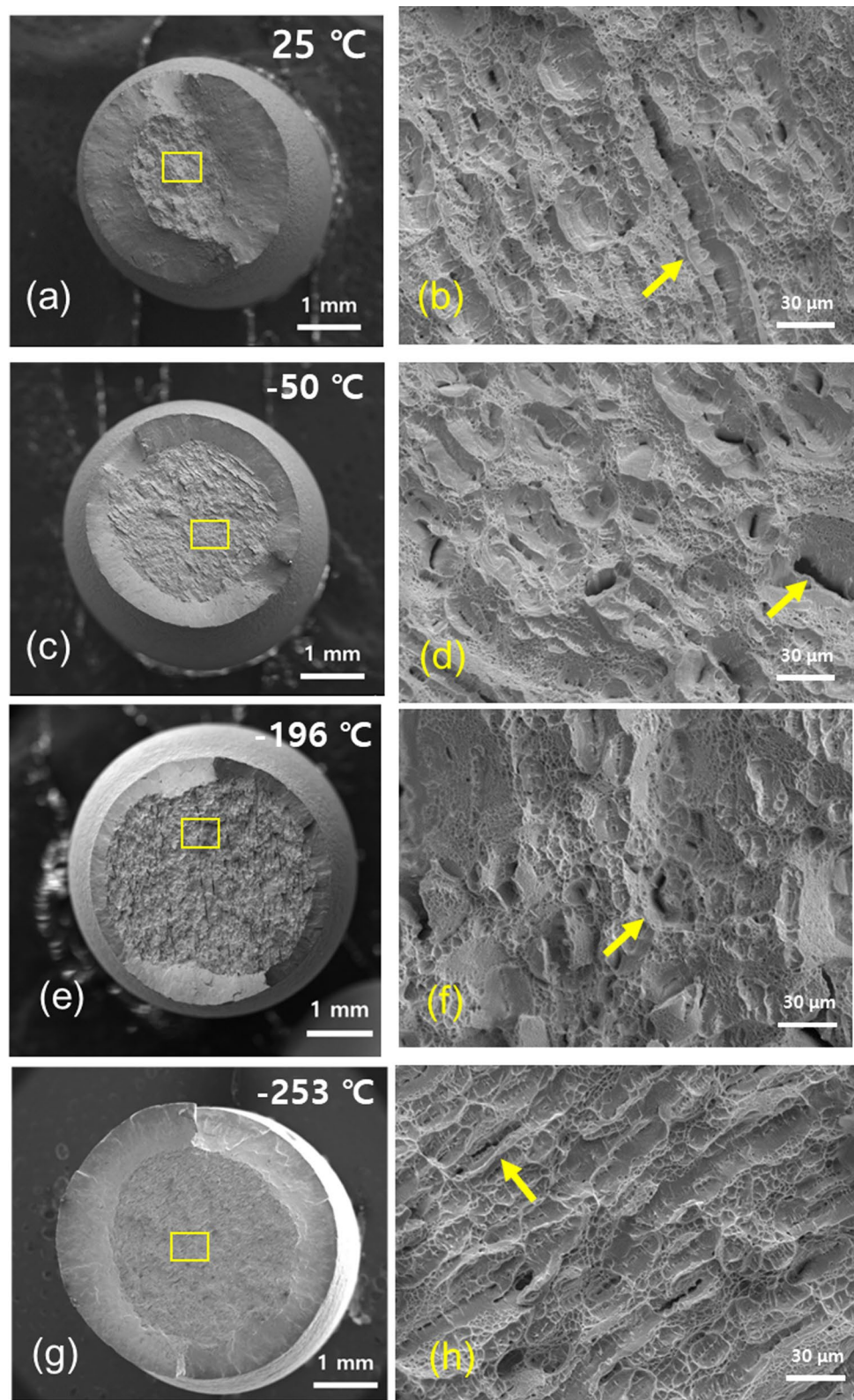
specimens were calculated (Fig. 10c). The $V_{\alpha'}$ values of H-uncharged specimens were 100%, except for the specimen deformed at 25 °C (56.3%). On the other hand, the $V_{\alpha'}$ values of H-precharged specimens, which were deformed at 25 °C, − 50 °C and − 100 °C, were 3.7%, 57.2%, and 94.2%, respectively. The $V_{\alpha'}$ values of H-precharged specimens deformed at temperatures below − 150 °C were 100%. The low $V_{\alpha'}$ values of H-precharged specimens were due to

Fig. 8 Side-longitudinal images and fracture surfaces of H-precharged specimens deformed at **a**, **b** 25 ℃, **c**, **d** − 50 ℃, **e**, **f** − 196 ℃ and **g**, **h** − 253 ℃. Yellow arrows in figures **b**, **d**, **f** and **h** indicate secondary cracks
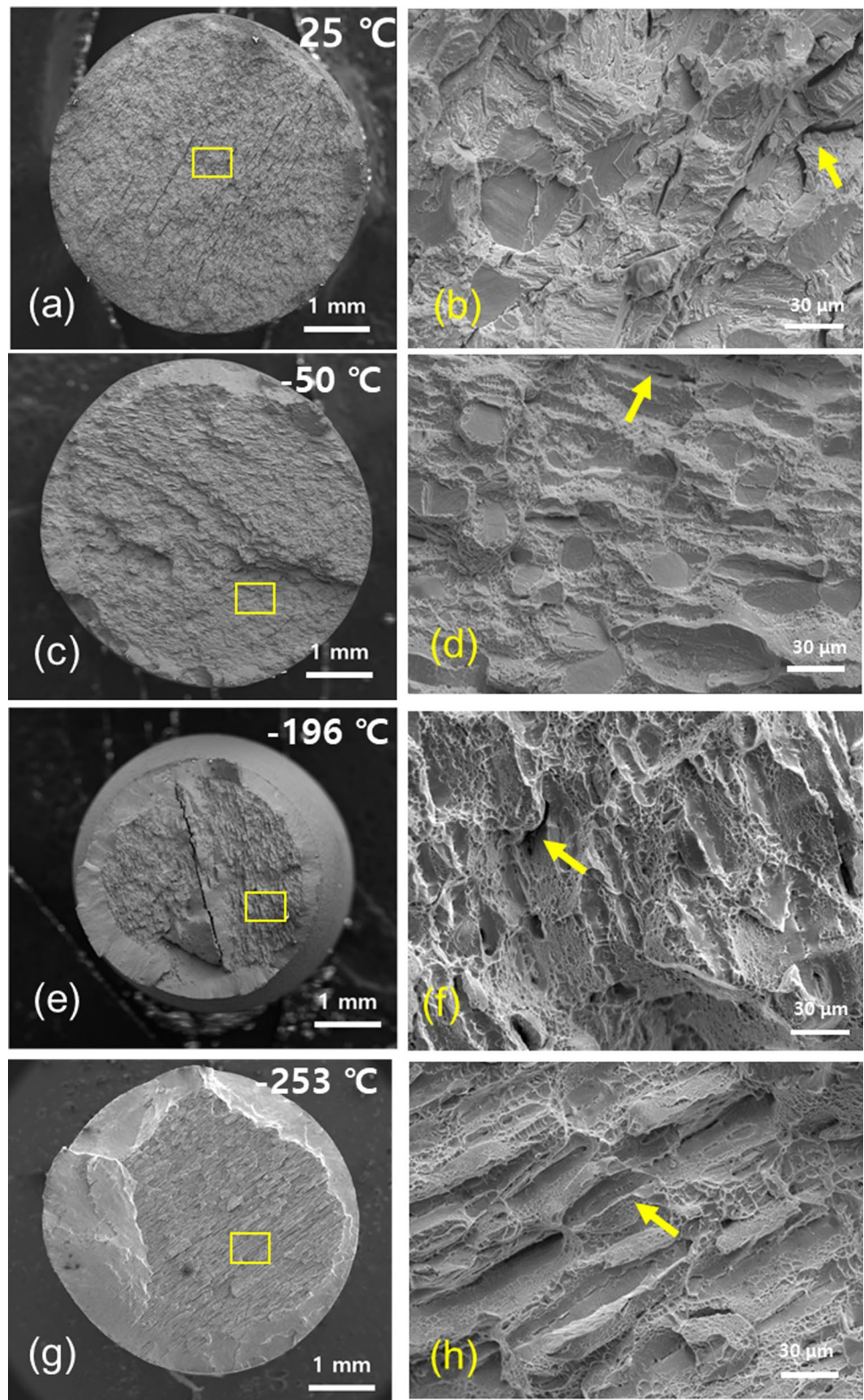
premature fracture caused by HE, as seen in Figs. 4 and 5c. Therefore, it was confirmed that SIMT becomes more active with decreasing tensile temperature in both H-uncharged and precharged specimens. This indicates that HE must be enhanced with decreasing tensile temperature due to the high volume fraction of brittle martensite. Accordingly, the absence of HE at low temperatures below ~ − 150 °C is not able to be explained by SIMT.
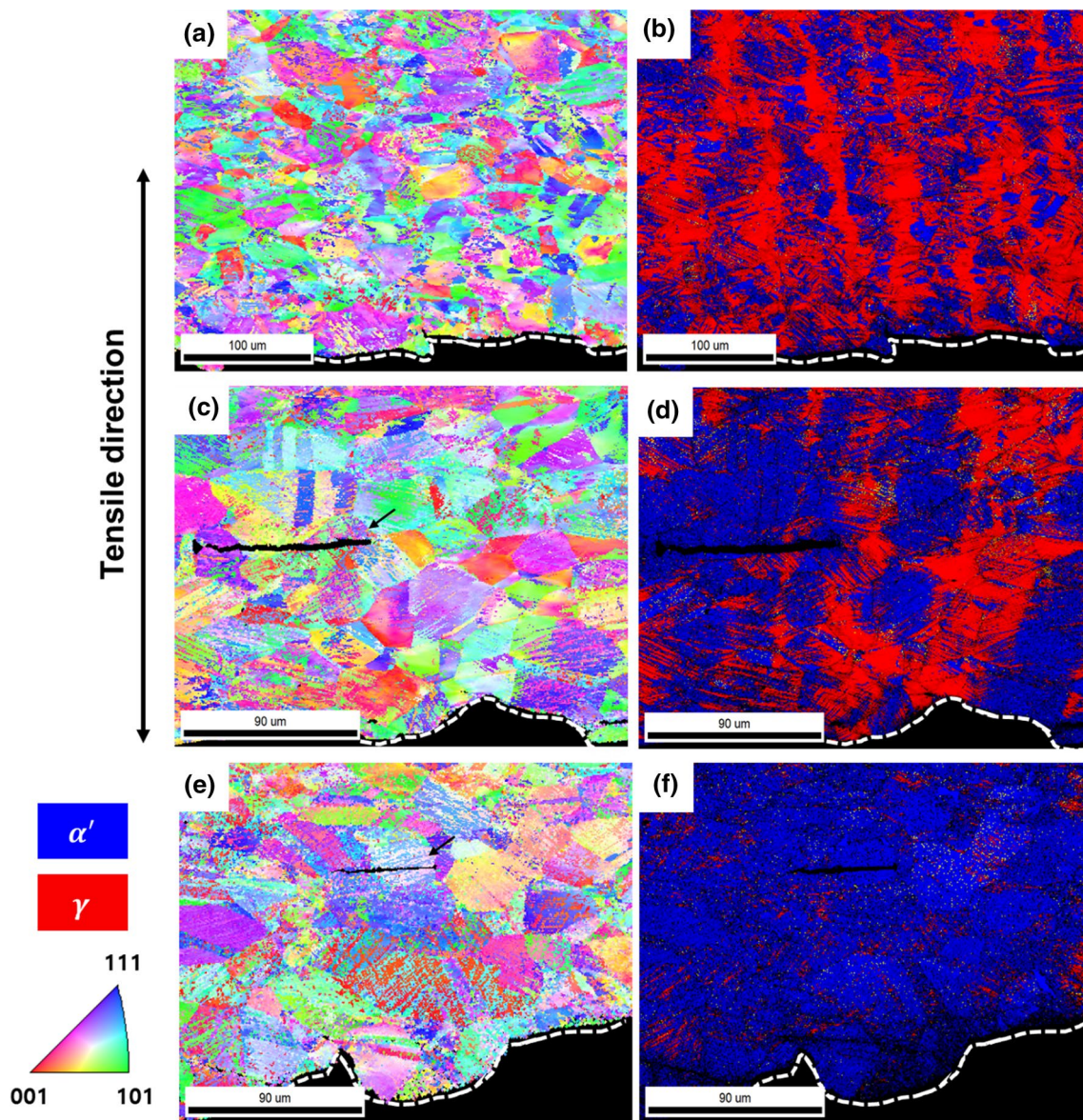
Fig. 9 EBSD inverse pole figure and phase maps taken near the fracture tip of H-precharged specimens deformed at **a, b** 25 ℃, **c, d** – 50 ℃ and **e, f** – 100 ℃

Thus, the H diffusivity (D_H) of STS 304 was examined. The D_H value of γ phase is $\sim 6.6 \times 10^{-16}$ m^2/s at 25 °C [22], and is expressed by Eq. (3) at the temperature range of 38–59 °C [23].

$$D_H(m^2/s) = 4.41 \times 10^{-7} \exp(-53500/RT) \qquad (3)$$

where R is the gas constant (8.314 J/mol K) and T is temperature (K).

Meanwhile, the D_H value of α' martensite of STS 304 is yet to be reported probably because STS 304 is known as an austenitic stainless steel. However, because it is important to examine the the D_H value of α' martensite of STS 304 to

explain the absence of HE at low temperatures, the D_H value of α' martensite of STS 304L was determined using two H permeation curves (Fig. 11) and Eq. (4), as mentioned in experimental procedure.

$$D_H = L^2 / (15.3 \times t_b) \qquad (4)$$

where L is the thickness of a specimen (0.7 mm for the 1st test and 0.65 mm for the 2nd test) and t_b is the breakthrough time, which is the time when $I/I_\infty = 0.1$ [24, 25] (141,560 s for the 1st test and 104,380 s for the 2nd test); I is current density, I_∞ is current density at the steady state.

Fig. 11 H permeation curves measured at 25 °C using an α' martensitic STS 304L specimen
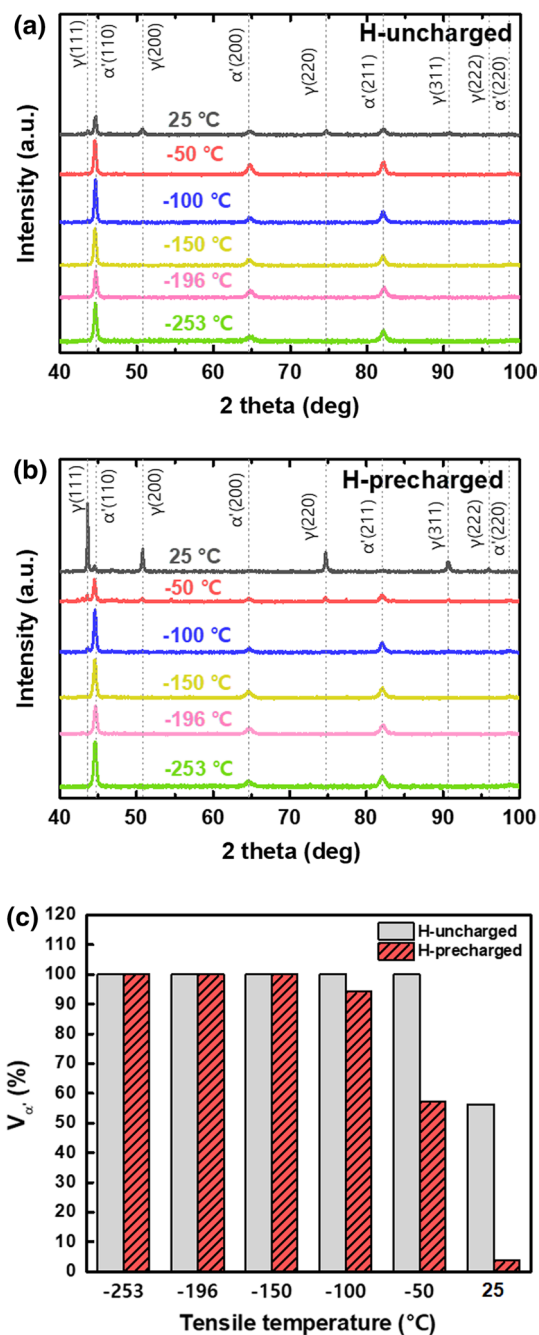

Fig. 10 X-ray diffraction patterns of **a** H-uncharged and **b** H-precharged specimens tensile fractured at various temperatures. **c** Volume fraction (%) of α' martensite of tensile-fractured H-uncharged and **b** H-precharged specimens

The I_∞ was determined as a current density where the current density starts to decrease with increasing time. After reaching a steady state, since an oxidation reaction occurs during the H detection process, a passivation film forms on the H detection surface, increasing the resistance of the surface. When the resistance increases, the current density decreases according to $V = IR$, which is known as the Ohmic
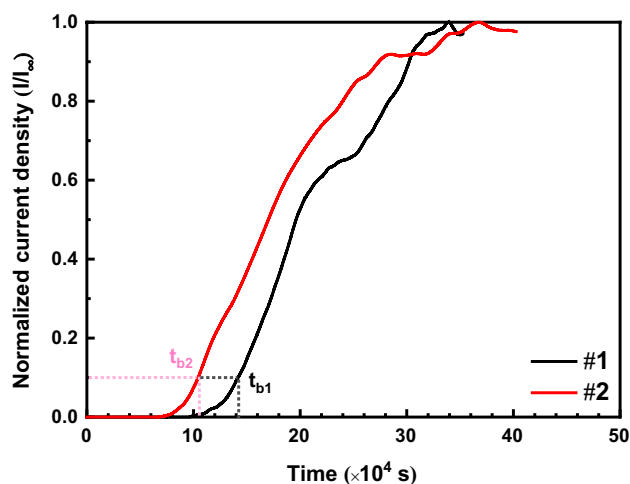
drop phenomenon [26]. In this study, the experiment was conducted for a long time due to the slow H diffusion rate, resulting in the formation of a passivation film on the H detection surface.

Finally, the D_H value of α' martensitic STS 304L, which was measured at 25 °C, is ~ 2.3×10^{-13} m^2/s for the 1st test and ~ 2.6×10^{-13} m^2/s for the 2nd test. Thus, the average D_H value is 2.45×10^{-13} m^2/s. However, strictly speaking the average D_H value is not highly accurate most likely due to a small fraction of γ (1.5%) and a passivation film on the H detection surface.

Figure 12a shows the temperature dependency of the D_H value in α ferritic steel [27], γ austenitic steel [27], γ austenitic STS 304L [27], tempered α' martensitic steel [28], and α' martensitic STS 304L used in this study. The measured and extrapolated D_H values are plotted in solid and dotted lines, respectively. The D_H value of austenitic STS 304L is lower than that of austenitic steel at the same temperature. The D_H value of martensitic STS 304L is lower those of ferritic and tempered martensitic steels. This is most likely due to the high content of Cr with a attractive force with H [29].

Assuming that the D_H value of α' martensitic STS 304L has the same temperature dependency as the D_H value of α ferritic steel [27] or tempered α' martensitic steel [27], the D_H values of α' martensitic STS 304L at 25 °C, − 50 °C, − 100 °C, − 150 °C and − 253 °C were obtained, and are plotted in Fig. 12b. The D_H values were reduced with decreasing temperature. In particular, the D_H value, obtained from tempered α' martensitic steel [28], was extremely low at temperatures below − 200 °C. Based on the D_H values and Eq. (5) [30], the diffusion distances of H (L_d) at temperatures mentioned above were calculated, and are also plotted in Fig. 12b.
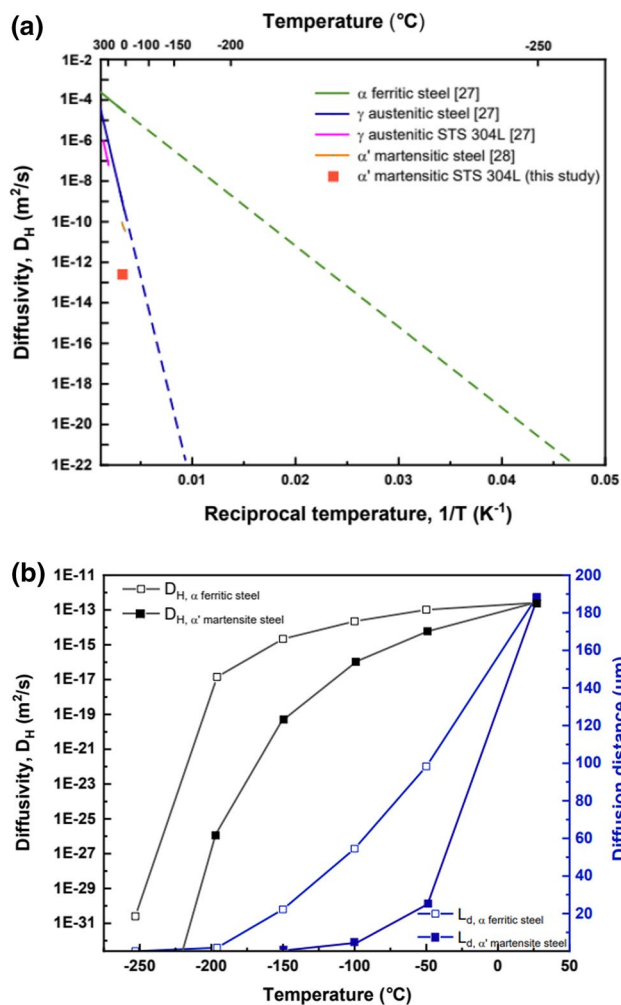
(a)

(b)

Fig. 12 **a** H diffusion coefficients in α ferritic steel, γ austenitic steel, γ austenitic STS 304L [27], α' martensitic steel [28] and α' martensitic STS 304L. Solid lines are calculated by experimental equation and dot lines are fitted. **b** D_H values and diffusion distance of α' martensitic STS 304L specimen plotted by α ferritic steel [27] and α' martensitic steel [28] at room temperature, -50 °C, -100 °C, -150 °C and -253 °C

$$L_d = \sqrt{6D_H t} \tag{5}$$

where t (s) is the deformation time, which elapsed until tensile fracture.

The L_d values at -150 °C, which were calculated with the D_H values obtained from α ferritic steel and tempered α' martensitic steel, turned out to be ~22.25 and ~0.11 mµ, respectively. Considering the facts that the average size of prior austenite grains was 26.3 mµ, the width of martensite laths is ~0.2–0.5 mµ [31, 32] and HE disappeared at -150 °C (Fig. 6b), the D_H value, determined based on tempered α' martensitic steel, is more reasonable compared to the D_H value obtained based on α ferritic steel. The absence of HE at temperatures below ~-150 °C is most likely due to the

difficulty in H diffusion to stress-concentrated regions inside brittle α' martensite.

5 Conclusion

In the present study, the resistance to HE of STS 304 was evaluated at a wide temperature range from 25 to -253 °C using thermally H-precharged specimens. The resistance to HE of H- precharged STS 304 was reduced with decreasing tensile temperature to ~-50 °C. However, as tensile temperature decreased further, the resistance to HE was improved again, finally HE disappeared at temperatures below ~-150 °C. The temperature dependency of the resistance to HE of H-precharged STS 304 is in accordance with that of STS 304 deformed in a H_2 gaseous atmosphere. Whereas HE occurred with assistance of SIMT and H diffusion at temperatures above ~-50 °C, it disappeared at low temperatures below ~-150 °C due to the sluggish H diffusion even in α' martensite, in spite of active SIMT.

Declarations

Conflict of interest The authors declar that they have no known competing financial interests or personal relationships that could have appeared to influence the work reported in this paper.

References

1. C. Zheng, W. Yu, Mater. Sci. Eng. A **710**, 359 (2018). https://doi.org/10.1016/j.msea.2017.11.003
2. J.B. Vogt, J. Foct, C. Regnard, G. Robert, J. Dhers, Metall. Trans. A **22**, 2385 (1991). https://doi.org/10.1007/BF02665004
3. N. Li, Y.D. Wang, W.J. Liu, Z.N. An, J.P. Liu, R. Su, P.K. Liaw, Acta Mater. **64**, 12 (2014). https://doi.org/10.1016/j.actamat.2013.11.001
4. B.H. Choe, S.W. Lee, J.K. Ahn, J. Lee, Korean J. Met. Mater. **58**, 583 (2020). http://dx.doi.org/10.3365/KJMM.2020.58.9.583
5. B.H. Choe, S.W. Lee, J.K. Ahn, J. Lee, T.W. Lim, Korean J Met. Mater. **58**, 653 (2020). http://dx.doi.org/10.3365/KJMM.2020.58.10.653
6. G. Han, J. He, S. Fukuyama, K. Yokogawa, Acta Mater. **46**, 4559 (1998). https://doi.org/10.1016/S1359-6454(98)00136-0
7. T. Michler, A.A. Yukhimchuk, J. Naumann, Corros. Sci. **50**, 3519 (2008). https://doi.org/10.1016/j.corsci.2008.09.025
8. D. Sun, G. Han, S. Vaodee, S. Fukuyama, K. Yokogawa, Mater. Sci. Technol. **17**, 302 (2001). https://doi.org/10.1179/026708301773002509
9. Y.H. Nam, J.S. Park, U.B. Baek, J.Y. Suh, S.H. Nahm, Int. J. Hydrog. Energy **44**, 7000 (2019). https://doi.org/10.1016/j.ijhydene.2019.01.065

10. T.T. Nguyen, J. Park, S.H. Nahm, N. Tak, U.B. Baek, Int. J. Hydrog. Energy. **44**, 28031 (2019). https://doi.org/10.1016/j.ijhydene.2019.08.233
11. ANSI/CSA CHMC 1-2014, Test methods for evaluating material compatibility in compressed hydrogen applications - Metals, CSA group (2014)
12. H. Addach, P. Bercot, M. Rezrazi, J. Takadoum, Corros. Sci. **51**, 263 (2009). https://doi.org/10.1016/j.corsci.2008.10.024
13. S.J. Kim, K.Y. Kim, Corros. Sci. Technol. **16**, 209 (2017). https://doi.org/10.14773/cst.2017.16.4.209
14. C.R. Hubbard, R.L. Snyder, Powder Diffr. **3**, 74 (1988). https://doi.org/10.1017/S0885715600013257
15. Y. Zhao, J.M. Park, D.H. Lee, E.J. Song, J.Y. Suh, U. Ramamurty, J.I. Jang, Scr. Mater. **168**, 76 (2019). https://doi.org/10.1016/j.scriptamat.2019.04.025
16. A.K. De, J.G. Speer, D.K. Matlock, D.C. Murdock, M.C. Mataya, R.J. Comstock, Metall. Mater. Trans. A **37**, 1875 (2006). https://doi.org/10.1007/s11661-006-0130-y
17. R. Kirchheim, Scripta Mater. **67**, 767 (2012). https://doi.org/10.1016/j.scriptamat.2012.07.022
18. N. Koga, T. Nameki, O. Umezawa, V. Tschan, K.P. Weiss, Mater. Sci. Eng. A **801**, 140442 (2021). https://doi.org/10.1016/j.msea.2020.1404422
19. B. Obst, A. Nyilas, Mater. Sci. Eng. A **137**, 141 (1991). https://doi.org/10.1016/0921-5093(91)90328-K
20. T. Ogata, T. Yuri, Y. Ono, Teion Kogaku **42**, 10 (2007). https://doi.org/10.2221/jcsj.42.10
21. Z.S. Basinski, Aust. J. Phys. **13**, 354 (1960). https://doi.org/10.1071/PH600354a
22. C. Zhou, Y. Song, Q. Shi, S. Hu, J. Zheng, P. Xu, L. Zhang, Int. J. Hydrog. Energy **44**, 26036 (2019). https://doi.org/10.1016/j.ijhydene.2019.08.046
23. Y. Sakamoto, H. Katayama, J. Jpn. Inst. Met. **46**, 805 (1982). https://doi.org/10.2320/jinstmet1952.46.8_805
24. A.M. Brass, A. Chanfreau, Acta Mater. **4**, 3823 (1996). https://doi.org/10.1016/1359-6454(95)00446-7
25. A. Oudriss, J. Creus, J. Bouhattate, E. Conforto, C. Berziou, C. Savall, X. Feaugas, Acta Mater. **60**, 6814 (2012). https://doi.org/10.1016/j.actamat.2012.09.004
26. E. Fallahmohammadi, F. Bolzoni, L. Lazzari, Int. J. Hydrog. Energy **38**, 2531 (2013). https://doi.org/10.1016/j.ijhydene.2012.11.059
27. G.R. Caskey Jr, in *Hydrogen Degradation of Ferrous Alloys*, ed. by R.A. Oriani, J.P. Hirth, M. Smialowski (Noyes Publications, Park Ridge, 1985), p. 822
28. S. Frappart, X. Feaugas, J. Creus, F. Thebault, L. Delattre, H. Marchebois, J. Phys. Chem. **71**, 1467 (2010). https://doi.org/10.1016/j.jpcs.2010.07.017
29. X.Y. Zhou, J.H. Zhu, Y. Wu, X.S. Yang, T. Lookman, H.H. Wu, Acta Mater. **224**, 117535 (2022). https://doi.org/10.1016/j.actamat.2021.117535
30. N.H. March, R.A. Street, M.P. Tosi (eds.), *Amorphous Solids and the Liquid State*, 1st edn. (Springer, New York, 1985), pp. 192–202
31. T. Maki, in *Phase Transformations in Steels*, ed. by E. Pereloma, D.V. Edmonds (Woodhead Publishing, Sawston, 2012), pp. 34
32. C. Sun, P. Fu, H. Liu, H. Liu, N. Du, Y. Cao, Cryst. **10**, 232 (2020). https://doi.org/10.3390/cryst10030232